Available online at www.sciencedirect.com
SCIENCE DIRECT®
International Journal of Heat and Mass Transfer 48 (2005) 5297–5309
International Journal of HEAT and MASS TRANSFER
www.elsevier.com/locate/ijhmt

A numerical study on the fluid flow and heat transfer in the confined jet flow in the presence of magnetic field

H.G. Lee [a], M.Y. Ha [b,*], H.S. Yoon [c]

[a] *Air Conditioning Division, LG Electronics Co., 76 Sungsan, Changwon, Republic of Korea*
[b] *School of Mechanical Engineering, Pusan National University San 30, Chang Jeon Dong, Kum Jeong Gu, Pusan 609-735, Republic of Korea*
[c] *Advanced Ship Engineering Research Center, Pusan National University San 30, Chang Jeon Dong, Kum Jeong Gu, Pusan 609-735, Republic of Korea*

Received 28 December 2004; received in revised form 20 July 2005
Available online 28 September 2005

Abstract

The present study numerically investigates two-dimensional fluid flow and heat transfer in the confined jet flow in the presence of applied magnetic field. For the purpose of controlling vortex shedding and heat transfer, numerical simulations to calculate the fluid flow and heat transfer in the confined jet are performed for different Reynolds numbers in the absence and presence of magnetic fields and for different Prandtl numbers of 0.02 (liquid metal), 0.7 (air) and 7 (water) in the range of $0 \leqslant N \leqslant 0.05$, where N is the Stuart number (interaction parameter) which is the ratio of electromagnetic force to inertia force. The present study reports the detailed information of flow and thermal quantities in the channel at different Stuart numbers. As the intensity of applied magnetic fields increases, the vortex shedding formed in the channel becomes weaker and the oscillating amplitude of impinging jet decreases. The flow and thermal fields become the steady state if the Stuart number is greater than the critical value. Thus the pressure coefficients and Nusselt number at the stagnation point representing the fluid flow and heat transfer characteristics also vary as a function of Stuart number.

1. Introduction

Impinging jets have been used in many industrial and engineering applications such as drying of papers, films and foods, freezing of tissue, tempering of glass and metal, cooling of gas turbine and combustor components, and cooling of electronic components, because of their capability to enhance or suppress the heat and mass transfer under relatively low pressure drops. The advantage of impinging jet flow is easy to adjust the location of interest and to remove a large amount of heat (or mass) on the impinging surface due to the thin hydrodynamic and thermal (or concentration) boundary layers around the stagnation region. In recent years, the power dissipation from the electrical and electronic components becomes larger because of their high density. The impinging jet is used as a promising candidate to remove more heat from the electrical and electronic components. However, in electronic packaging, because the space and size are limited, it is difficult to implement

* Corresponding author. Tel.: +82 51 510 2440; fax: +82 51 512 9835.
E-mail address: myha@pusan.ac.kr (M.Y. Ha).

0017-9310/$ - see front matter © 2005 Elsevier Ltd. All rights reserved.
doi:10.1016/j.ijheatmasstransfer.2005.07.025

Nomenclature

B_0	external magnetic field
C_f	friction coefficient $(\tau_w/\frac{1}{2}\rho V_{jet}^2)$
C_p	pressure coefficient $[(p_x - p_{jet})/\frac{1}{2}\rho V_{jet}^2]$
D	jet nozzle width
f_x, f_y	Lorentz forces in x and y direction
H	nozzle-to-plate spacing
L	channel length
n	normal direction to the wall
N	Stuart number or interaction parameter
Nu	local Nusselt number
p	dimensionless pressure
Pr	Prandtl number
Re	Reynolds number ($V_{jet}D/\nu$)
t	dimensionless time
t_p	period of time integration
T	dimensionless temperature
T_w	bottom wall temperature
T_{jet}	nozzle exit temperature
u, v	dimensionless velocity in x and y direction
V_{jet}	nozzle exit velocity
x, y	Cartesian coordinates

Greek symbols

α	thermal diffusivity
ρ	density
σ	electric conductivity
ν	kinematic viscosity
ϕ	electrical potential
τ_w	wall shear stress

Subscripts/superscripts

RMS	root mean square
stag	stagnation point
w	bottom wall
*	dimensional value
¯	time-averaged quantity
jet	jet

properly the impinging jet which works at the low Reynolds number under low operating pressure condition.

There have been many experimental and numerical studies to investigate the flow structures and heat transfer mechanisms in detail to obtain the optimal operating conditions of impinging jet for different industrial and engineering applications [1–12]. Sparrow and Wong [1] derived the mass transfer correlation for the impinging slot-jet flows at the Reynolds number of $150 < Re < 950$ using the naphthalene sublimation technique and the analogy of heat and mass transfer. Bouainouche et al. [2] carried out the numerical study based on the RANS method to predict the wall shear stress produced by a normal impinging thin plane turbulent jet on a flat plate. They compared their computational results obtained using different wall functions in their turbulence model with experimental data and proposed a hybrid law to predict the measured wall shear stress well in the impinging region. Chen et al. [3] carried out the experimental and numerical study to investigate the high Schmidt-number mass transfer to a line electrode in laminar impinging slot-jet flows for the slot-based Reynolds number from 220 to 690. Their experimental and theoretical results show that the peak values in mass transfer occur at a point one-half to one jet width away from the stagnation point, which was not observed by the earlier studies. Beitelmal et al. [4] performed an experimental study to determine the effect of the inclination of an impinging two-dimensional air jet on the heat transfer from a uniformly heated flat plate. They determined the local Nusselt number as a function of three parameters: (a) inclination angle of the air jet relative to the plate in the range of 90–40°, (b) nozzle exit-to-plate spacing (z/D) in the range of 4–12 and (c) Reynolds number based on the hydraulic diameter of the slot nozzle in the range of 4000–12,000. Phares et al. [5] presented a method for the theoretical determination of the wall shear stress under impinging jets of the wide range of Reynolds numbers and jet heights. They compared their theoretically predicted results with available wall shear stress measurements and found that the electrochemical method in submerged impinging liquid jets could predict the wall shear stress in the impingement region most accurately among any indirect methods and determine an empirical relation describing the rise in wall shear stress due to compressibility effects in impinging high-velocity jets. Chattopadhyay and Saha [6] investigated turbulent flow fields and heat transfer from an array of impinging horizontal knife jets on a moving surface using large eddy simulation (LES) with a dynamic subgrid stress model for various surface velocities directed perpendicular to the jet plane. They found that performance of the knife jet was better for a surface-velocity-to-nozzle-exit-velocity ratio of 0.5 and with increasing plate speed, Nu distribution tends to be more uniform although the total heat transfer reduces. Hwang et al. [7] conducted an experimental study to investigate the effect of vortex pairing, which was generated by the two methods of secondary shear flow and acoustic excitation, on the flow and heat transfer characteristics of an impinging jet. The control of vortex pairing enhanced or reduced heat transfer from the impinging surface because of the change of flow structures. Choo and Kang [8] measured directly the local velocities of the liquid

sheet formed by two low-speed impinging jets using a LDV. They investigated the spatial distribution of the local sheet velocity as well as the effects of the impingement angle and jet velocity on the sheet velocity. Aldabbagh and Sezai [9] investigated the flow and heat transfer characteristics of impinging laminar multiple square jets through the solution of the three-dimensional Navier–Stokes and energy equations in steady state for different jet-to-jet spacings and nozzle exit to plate distances. Chiriac and Ortega [10] computed the steady and unsteady flow and heat transfer due to a confined two-dimensional slot jet impinging on an isothermal plate using a numerical finite-difference approach for different Reynolds numbers in the range of 250–750 at the fixed Prandtl number of 0.7 and jet-to-plate spacing of 5. The flow and heat transfer at the Reynolds numbers of 250 and 350 were steady whereas those at the Reynolds number of 750 was unsteady and showed very complex pattern with buckling, flapping and sweeping of the jet due to vortex shedding and a non-linear interaction between the jet and the channel fluid. The stagnation Nusselt number is directly proportional to the jet Reynolds number at the steady state condition, whereas those at the unsteady condition are less dependent on the Reynolds number. Chung et al. [11] performed direct numerical simulations of an unsteady impinging jet to study momentum and heat transfer characteristics by solving the unsteady compressible Navier–Stokes equations using a high-order finite difference method with non-reflecting boundary conditions. They investigated the effect of primary and secondary vortices on the local heat transfer and fluid flow. Beaubert and Viazzo [12] computed the flow field of plane impinging jets at moderate Reynolds numbers using large eddy simulation technique with the dynamic Smagorinsky model for two Reynolds numbers of 3000 and 7500. They calculated the instantaneous, mean values and turbulence statistics for dependent variables to investigate the fluid flow and heat transfer characteristics in detail. Chattopadhyay and Saha [13] computed the flow field due to an impinging jet over a moving surface at a moderately high Reynolds number emanating from a rectangular slot nozzle using the large eddy simulation technique with a dynamic subgrid-scale stress model. They calculated turbulence quantities such as kinetic energy, production rate of turbulent kinetic energy and the Reynolds stress for different surface velocities to provide an insight into the impinging jet turbulent flow.

Most of these previous researches are related to the study to investigate experimentally and numerically the fluid flow and heat transfer characteristics for various types of impinging jets in the absence of applied magnetic fields. There are little studies to consider the effect of applied magnetic fields on the fluid flow and heat transfer of impinging jet in detail. One possible application is the molten steel flow control using the electromagnetic brake (EMBR) system in a continuous casting process, because the flow coming from the entry nozzle submerged in the molten steel is very similar to the impinging jet flow [14]. The EMBR is widely used in a field of steel manufacturing.

In the present study, we investigated the effects of magnetic fields on the fluid flow and heat transfer of the confined impinging jet. We obtained the numerical solutions for unsteady two-dimensional governing equations for the fluid flow and heat transfer using the finite volume method. We calculated the instantaneous velocity vector and isothermal lines, time-averaged wall friction and pressure coefficients along the impinging wall, and time-averaged pressure coefficient and Nusselt number at the stagnation point as a function of the magnitude of applied magnetic fields. The results obtained for the case with applied magnetic fields are compared with those without magnetic fields.

2. Governing equations

Fig. 1 shows the computational domain and coordinate system for a two-dimensional confined impinging jet considered in the present study. We solve the unsteady two-dimensional dimensionless continuity, Navier–Stokes and energy equations defined as

$$\nabla \cdot \vec{u} = 0 \tag{1}$$

$$\frac{\partial \vec{u}}{\partial t} + \vec{u} \cdot \nabla \vec{u} = -\nabla p + \frac{1}{Re} \nabla^2 \vec{u} + \vec{f} \tag{2}$$

$$\frac{\partial T}{\partial t} + \vec{u} \cdot \nabla T = \frac{1}{Re \cdot Pr} \nabla^2 T \tag{3}$$

The dimensionless variables in the above equations are defined as

$$t = \frac{V_{\text{jet}} t^*}{D}, \quad \vec{u} = \frac{\vec{u}^*}{V_{\text{jet}}}, \quad p = \frac{p^*}{\rho V_{\text{jet}}^2}, \quad T = \frac{T^* - T_{\text{w}}}{T_{\text{jet}} - T_{\text{w}}} \tag{4}$$

In the above equations, ρ, V_{jet}, T_{jet}, T_{w}, and D represent the density, inlet jet velocity, inlet jet temperature, bottom wall temperature and jet width. The superscript * in Eq. (4) represents the dimensional variables. $\vec{u}$, T, p, and t are the non-dimensional velocity vector, temperature, pressure and time. The above non-dimensionalization results in two dimensionless parameters: $Re = V_{\text{jet}} D/\nu$ and $Pr = \nu/\alpha$ where ν and α are the kinematic viscosity and thermal diffusivity. In the simulations to be reported here the Prandtl number, Pr, has been taken to be 0.02, 0.7 and 7 corresponding to liquid metal, air and water, respectively. $Pr = 0.7$ is corresponding to air which is not electrically conducting. However, $Pr = 0.7$ is considered as just an intermediate numerical value in order to demonstrate the tendency for increasing Pr. The purpose of the present study is to investigate the effects of applied magnetic fields on the impinging jet

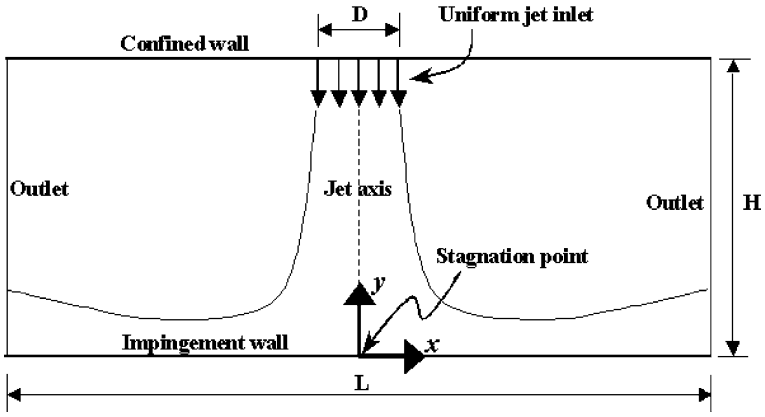

Fig. 1. Computational domain and coordinate system for a two-dimensional confined impinging jet.

flow and as a result the effect of buoyancy is ignored in the present study. We limit attention to the case of incompressible flow of constant thermodynamic and transport property for the fluid. We also assume that the flow is two-dimensional and invariant along the spanwise direction for the low Reynolds numbers considered in the present problem.

We assume that the magnetic field is parallel to the z-direction with constant values and as a result the Lorentz force $\vec{f}$ used in Eq. (2) and acting on the fluid is defined as follows [14–16]:

$$\vec{f} = N(\vec{J} \times e_z) \tag{5}$$

$$\nabla \cdot \vec{J} = 0 \tag{6}$$

$$\vec{J} = -\nabla\phi + \vec{u} \times e_z \tag{7}$$

$$\nabla^2\phi = \nabla \cdot (\vec{u} \times e_z) \tag{8}$$

Using Eqs. (6) and (7), we can derive a Poisson equation (8). The Poisson equation is solved to get the electric potential ϕ. The Lorentz force in the momentum Eq. (2) induced by the magnetic field is obtained by using Eq. (5). Here we can define additional dimensionless parameter called as Stuart number or interaction parameter, which is the ratio of electromagnetic force to inertia force, as follows:

$$N = \sigma B_0^2 D/(\rho V_{\text{jet}}) \tag{9}$$

where σ and B_0 represent electric conductivity and external magnetic field.

3. Numerical methodology

The central difference scheme with the second-order accuracy based on the finite volume method is used for the spatial discretization. A two-step time-split scheme is used to advance the flow field. First the velocity is advanced from time level 'n' to an intermediate level by solving the advection–diffusion equation. In the advection-diffusion step, the non-linear terms are treated explicitly using third-order Adams–Bashforth scheme. The diffusion terms are treated implicitly using Crank–

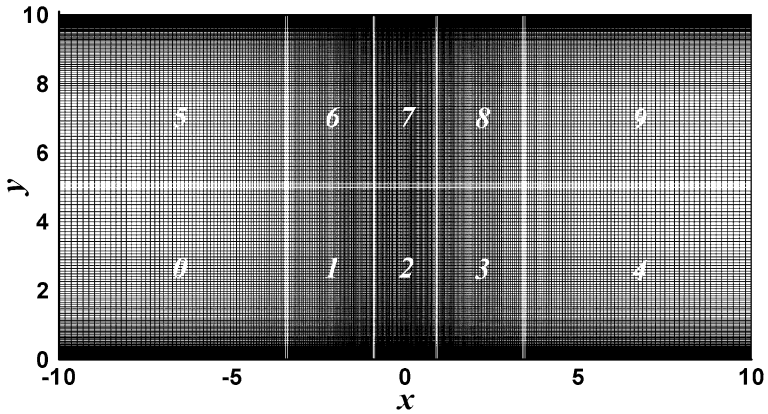

Fig. 2. Grid distribution and the number of domain used.

Nicolson scheme. Then a Poisson equation for pressure is solved fully implicitly. The final divergence-free velocity field at '$n+1$' is obtained with a pressure-correction step. The temperature field is advanced in a similar manner with third-order Adams–Bashforth scheme for the advection term and Crank–Nicolson scheme for the diffusion term [17].

The boundary conditions used in the present study are defined as

$$\begin{aligned}
&\text{Inlet}: u=0, \quad v=-1, \quad T=1\\
&\text{Upper wall}: u=v=0, \quad \frac{\partial T}{\partial n}=0\\
&\text{Lower wall}: u=v=0, \quad T=0\\
&\text{Lateral exit}: \frac{\partial u}{\partial t}+C\frac{\partial u}{\partial x}=0, \quad \frac{\partial T}{\partial t}+C\frac{\partial T}{\partial x}=0
\end{aligned} \tag{10}$$

where C represents a mean value of velocities at the lateral exits.

Fig. 2 shows the grid distribution and the number of domain used in the present study. The number of grid points used in the present calculation is $301\times 201(x\times y)$ and the number of domain used is 10. Grid independence of the solution has been confirmed with additional simulations on much less and finer grids. The condition of CFL < 0.3 is chosen to determine the non-dimensional time step used in the present calculations. The computations are advanced in time until it is observed that the pressure and heat transfer coefficients have reached a statistically stationary state. The developed computer code is parallelized based on the message passing interface (MPI) to increase the computational speed [18]. The number of processors used is 5 in the x-direction and 2 in the y-direction, respectively, as shown in Fig. 2. The same number of grid points is allocated to each processor.

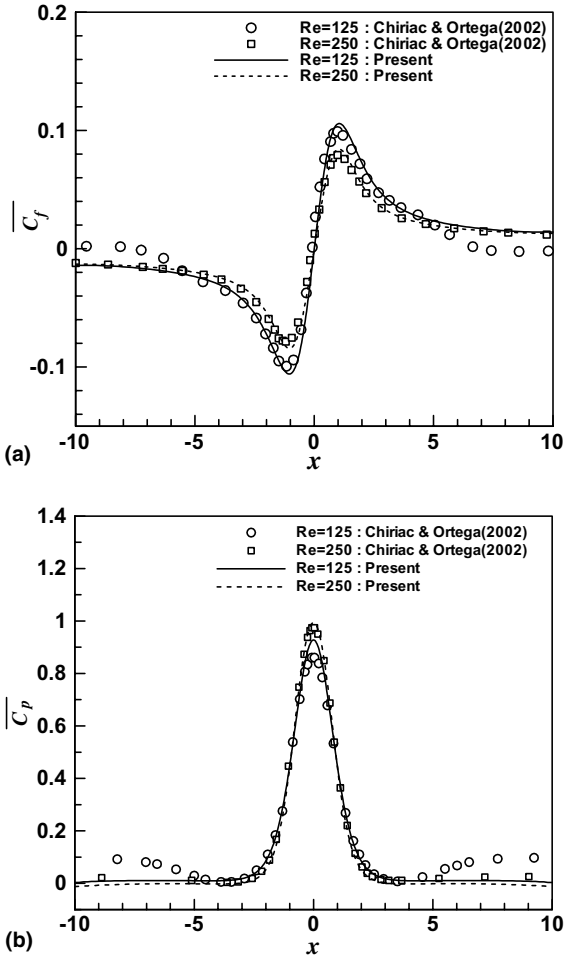

Fig. 3. Time-averaged wall friction and pressure coefficients ($\overline{C}_f$ and $\overline{C}_p$) along the lower wall at $H/D=5$, $Re=125$ and 250 in the absence of applied magnetic fields.

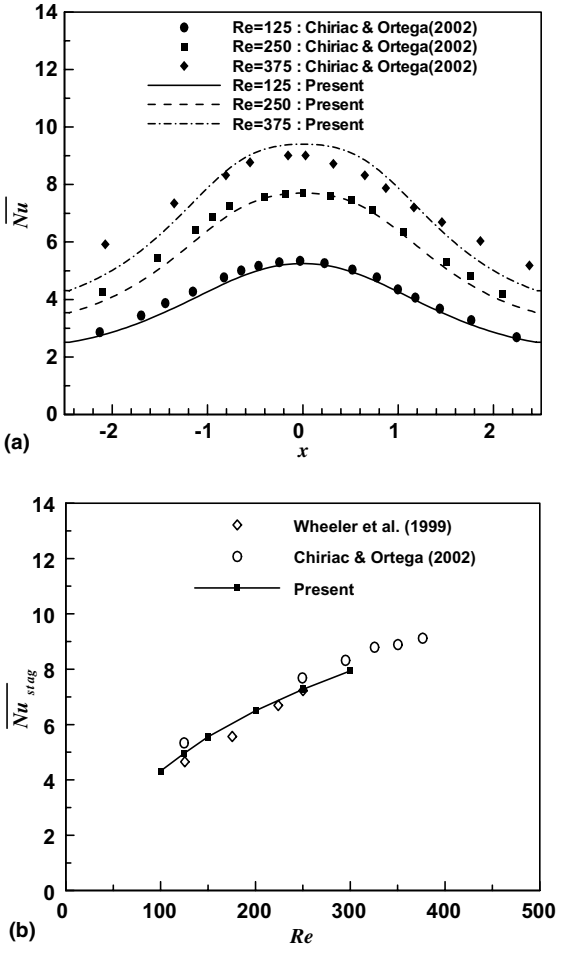

Fig. 4. Time-averaged Nusselt number along the lower wall ($\overline{Nu}$) and time-averaged Nusselt number at the stagnation point ($\overline{Nu}_{\text{stag}}$) for different Reynolds number of 125, 250 and 375 at $H/D=5$ in the absence of applied magnetic fields.

Once the velocity and temperature fields are obtained, the local and time-averaged Nusselt number are defined as

$$Nu = \left.\frac{\partial T}{\partial n}\right|_{\text{wall}} \qquad \overline{Nu} = \frac{1}{t_p}\int_0^{t_p} Nu\,\mathrm{d}t \tag{11}$$

where n is the normal direction to the walls and t_p is the period of time integration.

4. Results and discussion

For the purpose of validation study of the present computational results, the fluid flow and heat transfer for the confined impinging jet without an applied magnetic field was tested for different Reynolds numbers and their results are compared with the previous results [10]. Fig. 3 shows the time-averaged wall friction and pressure coefficients ($\overline{C}_f$ and $\overline{C}_p$) along the lower wall for the case without the applied magnetic fields when $H/D = 5$ at $Re = 125$ and 250. The present predicted results for $\overline{C}_f$ and $\overline{C}_p$ represent well the results computed by Chiriac and Ortega [10]. Fig. 4 shows the time-averaged Nusselt number along the lower wall ($\overline{Nu}$) and time-averaged Nusselt number at the stagnation point ($\overline{Nu}_{\text{stag}}$) for different Reynolds numbers for the case without the applied magnetic fields when $H/D = 5$. The present predicted results for the time-averaged Nusselt number along the lower wall and the time-averaged Nusselt number at the stagnation point also represent well the results computed by Chiriac and Ortega [10]. Even though the present validation study shows generally a good agreement between the present computational results and those of Chiriac and Ortega [10] for $\overline{C}_f$, $\overline{C}_p$, $\overline{Nu}$ and $\overline{Nu}_{\text{stag}}$ as shown in Figs. 3 and 4, we can observe some minor discrepancy between two numerical results in the regions far from centerline. This discrepancy might occur due to the difference in the number of grid points and computational times used in two different studies. The number of grid points used in the present study is 301×201 in the x- and y-direc-

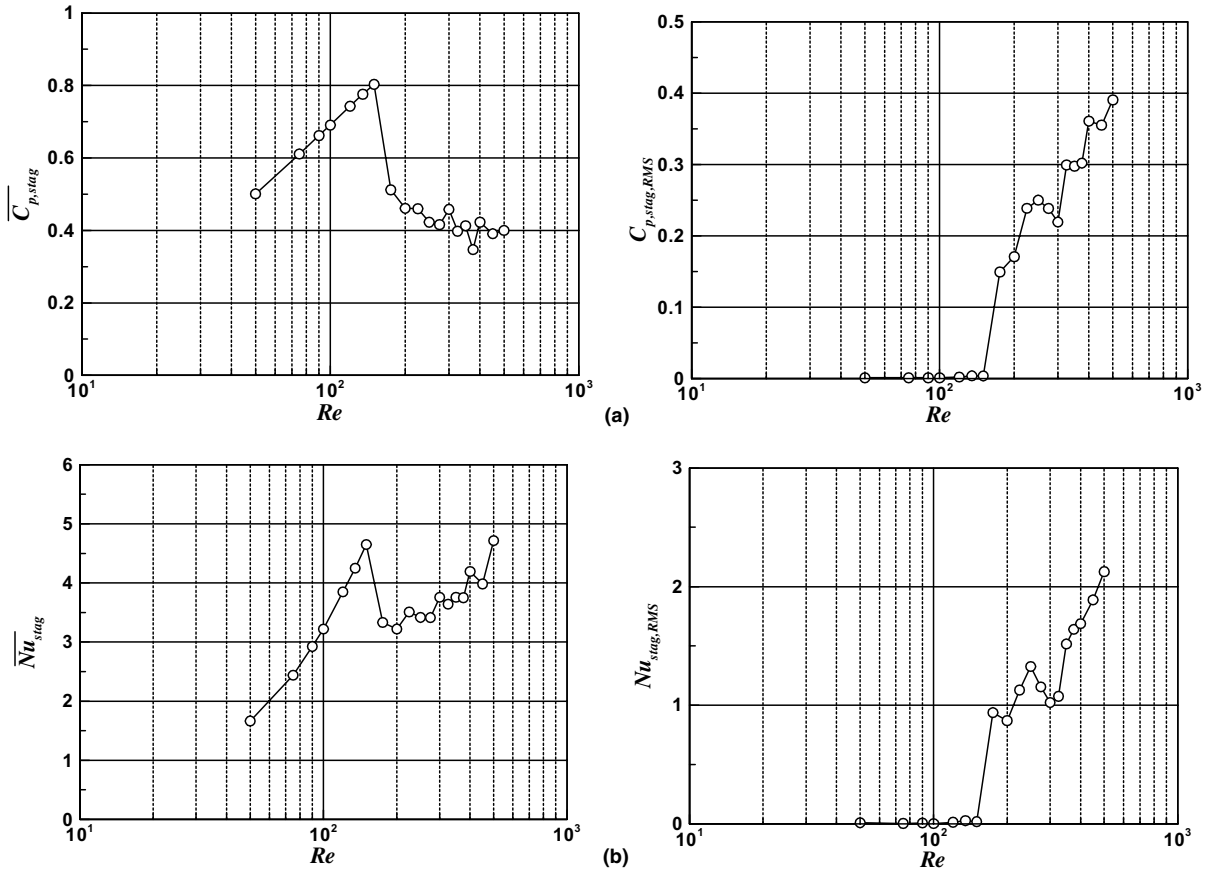

Fig. 5. Time-averaged and root-mean-square values of pressure coefficients ($\overline{C}_{p,\text{stag}}$) and Nusselt number at the stagnation point ($\overline{Nu}_{\text{stag}}$) as a function of Reynolds number at $H/D = 10$ and $Pr = 0.7$ in the absence of applied magnetic fields.

tions, respectively, whereas the maximum number of grid points used by Chiriac and Ortega [10] is 116×86. Thus our present computational results have higher resolution than those by Chiriac and Ortega [10]. For the viewpoint of computational time, the discrepancy between the two results is very small when we carry out the computation for a short time period. However, we can observe some minor discrepancy in the regions far from the centerline between two numerical results when we carry out for a longer time period. So we conjecture that the computational times used by Chiriac and Ortega [10] may not be long enough.

Fig. 5 shows the time-averaged and root-mean-square values of pressure coefficient, $\overline{C}_{p,\mathrm{stag}}$, and Nusselt number at the stagnation point, $\overline{Nu}_{\mathrm{stag}}$, as a function of Reynolds number for the case without the applied magnetic fields at $H/D = 10$ and $Pr = 0.7$. When $50 \leqslant Re \leqslant 150$, the fluid flow and heat transfer are steady, and $\overline{C}_{p,\mathrm{stag}}$ and $\overline{Nu}_{\mathrm{stag}}$ increase as the Reynolds number increases. If the Reynolds number increases from 150 to 175, the fluid flow and heat transfer change their mode from the steady state to the unsteady one, and $\overline{C}_{p,\mathrm{stag}}$ and $\overline{Nu}_{\mathrm{stag}}$ decrease very rapidly. When $Re \geqslant 175$, the fluid flow and temperature fields still become time-dependent and the root-mean-square values of $\overline{C}_{p,\mathrm{stag}}$ and $\overline{Nu}_{\mathrm{stag}}$ increases due to increasing unsteadiness with increasing Reynolds number. The values of $\overline{C}_{p,\mathrm{stag}}$ keep decreasing slowly with increasing Reynolds number at $Re \geqslant 175$, compared to the rapid decrease in $\overline{C}_{p,\mathrm{stag}}$ when the Reynolds number increases from 150 to 175. When $Re \geqslant 175$, the values of $\overline{Nu}_{\mathrm{stag}}$ have the minimum value at $Re = 200$ and then increases again with increasing Reynolds number. The slope of increasing $\overline{Nu}_{\mathrm{stag}}$ at $Re \geqslant 200$ is lower than that at $50 \leqslant Re \leqslant 150$.

Fig. 6 shows the instantaneous velocity vectors at $Re = 250$ and $H/D = 10$ for different N values in the

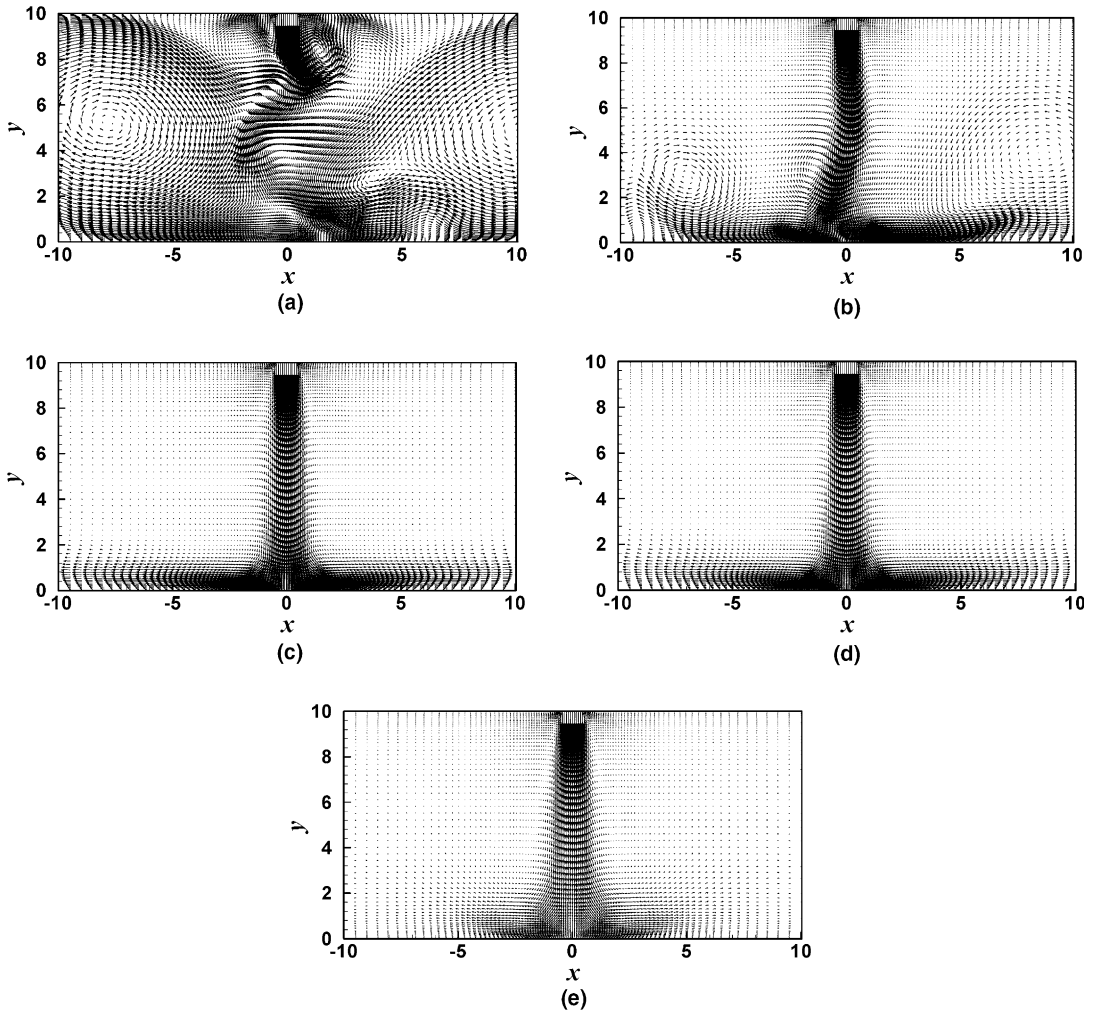

Fig. 6. Instantaneous velocity vectors at $Re = 250$ and $H/D = 10$ for different N values. (a) $N = 0$, (b) $N = 0.0025$, (c) $N = 0.005$, (d) $N = 0.01$ and (e) $N = 0.03$.

presence of magnetic fields. Fig. 6(a) shows the instantaneous velocity vector for $N = 0$ corresponding to the case without the applied magnetic field to compare its results with those for the case in the presence of magnetic fields. For $N = 0$, the jet flow is highly time-dependent and the symmetry of the flow is broken. The jet core is distorted, and the primary vortices emanating from the jet shear layer are alternately shed on both sides of the jet. As the flow is deflected from the wall after the jet impinges on the lower wall, a wall jet is developed. The wall jet flow is separated from the wall because the flow is retarded by the wall shear stress. The detached wall jet flow is partially re-entrained into the jet, forms a pair of recirculating zones and interacts with the primary vortices, giving rise to very complex unsteady vortical motions as shown in Fig. 6(a). If the constant magnetic fields are applied to the confined impinging jet in the z-direction, the forces defined by Eq. (5) can be expressed as for the present two-dimensional problem:

$$f_x = -N\left(\frac{\partial \phi}{\partial y} + u\right), \quad f_y = -N\left(-\frac{\partial \phi}{\partial x} + v\right) \tag{12}$$

Thus the forces induced by the magnetic fields act on the jet flow in the opposite direction and damp the movement of jet flow. When $N = 0.0025$ corresponding to the weak magnetic field, the instantaneous flow field is still time-dependent and shows a non-symmetric pattern similar to the case of $N = 0$. However, the extent of unsteady behavior is greatly decreased when N increases from 0 to 0.0025. If N is increased further to 0.005, the unsteadiness of flow is very weak. As a result the jet flow approaches to the steady state and shows almost the symmetric pattern. When the magnetic field is strong as $N \geqslant 0.01$, the jet flow becomes steady and symmetric. The pattern of jet flow for $N \geqslant 0.01$ is very

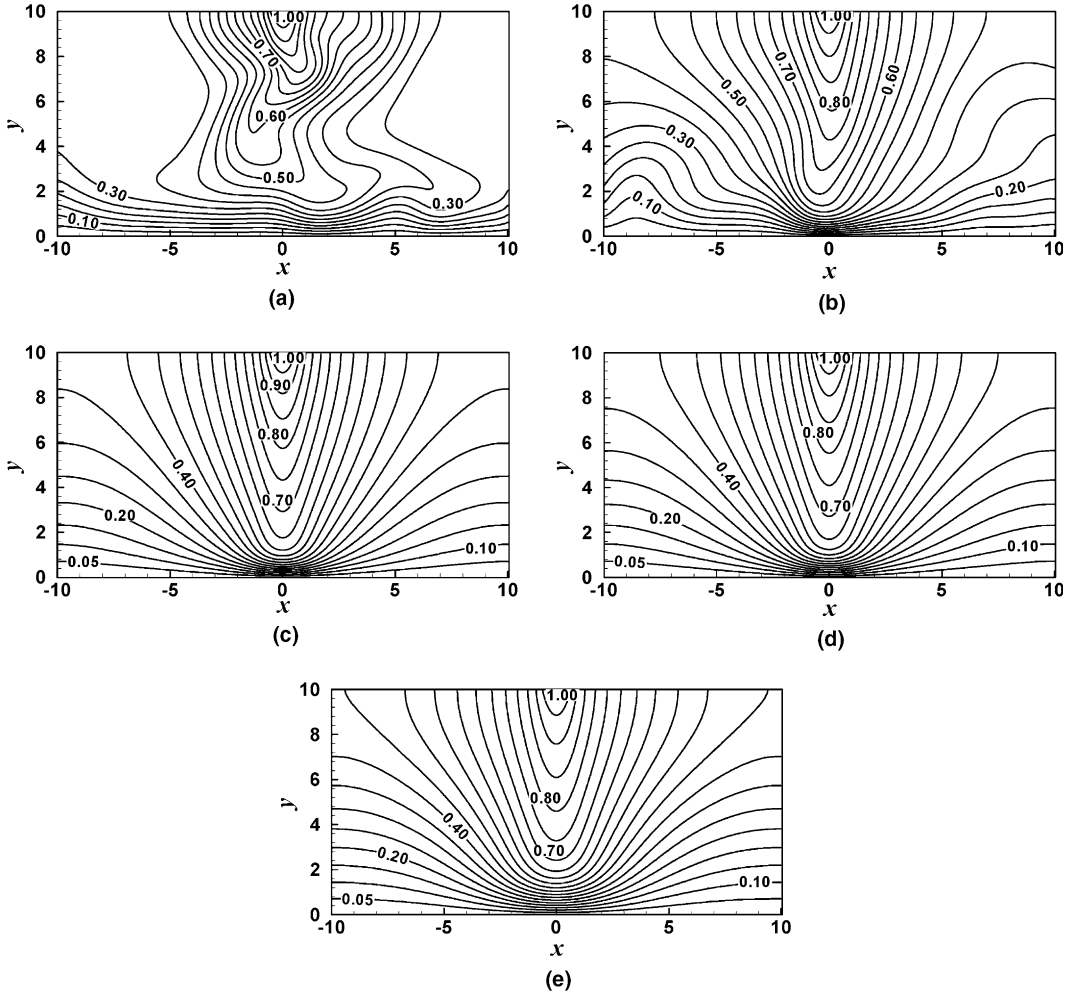

Fig. 7. Instantaneous temperature fields at $Re = 250$, $Pr = 0.02$ and $H/D = 10$ for different N values. (a) $N = 0$, (b) $N = 0.0025$, (c) $N = 0.005$, (d) $N = 0.01$ and (e) $N = 0.03$.

similar to that of steady jet flow obtained at the lower Reynolds number. When $N = 0.03$, the applied magnetic field is so strong that the jet flow cannot arrive at the stagnation point at the lower wall at the Reynolds number of 250 due to the strong Lorentz force.

Figs. 7–9 show the distribution of instantaneous dimensionless temperature fields for different Stuart numbers of $N = 0$–0.03 and different Prandtl numbers of $Pr = 0.02$, 0.7 and 7 at $H/D = 10$ and $Re = 250$. The thermal gradient and heat transfer rate on the lower wall increases with increasing Prandtl number for both cases with and without the applied magnetic fields. When $N < 0.005$, the temperature fields are time-dependent and non-symmetric with respect to the vertical centerline with shedding phenomena, because the flow is time-dependent at these Stuart numbers as shown in Fig. 6. When $Pr = 0.02$, because the thickness of thermal boundary layer is much larger than that of velocity boundary layer, the temperature fields are not much affected by the velocity fields and the thickness of thermal boundary layers formed on the lower wall and along the centerline is large. As a result, the temperature fields are widely distributed in the whole region of channel with relatively small temperature gradient and we can observe the relatively weak unsteadiness compared to the complex and strong unsteady flow fields. When the Prandtl number increases to 0.7 at $N < 0.005$, the temperature fields follow the flow fields because the thickness of thermal boundary layer has almost the same order of magnitude as that of hydraulic boundary layer. Thus the temperature fields at $Pr = 0.7$ show a very complex and unsteady pattern when $N < 0.005$, compared to those at $Pr = 0.02$. The thermal boundary layers formed along the centerline and on the lower wall for $Pr = 0.7$

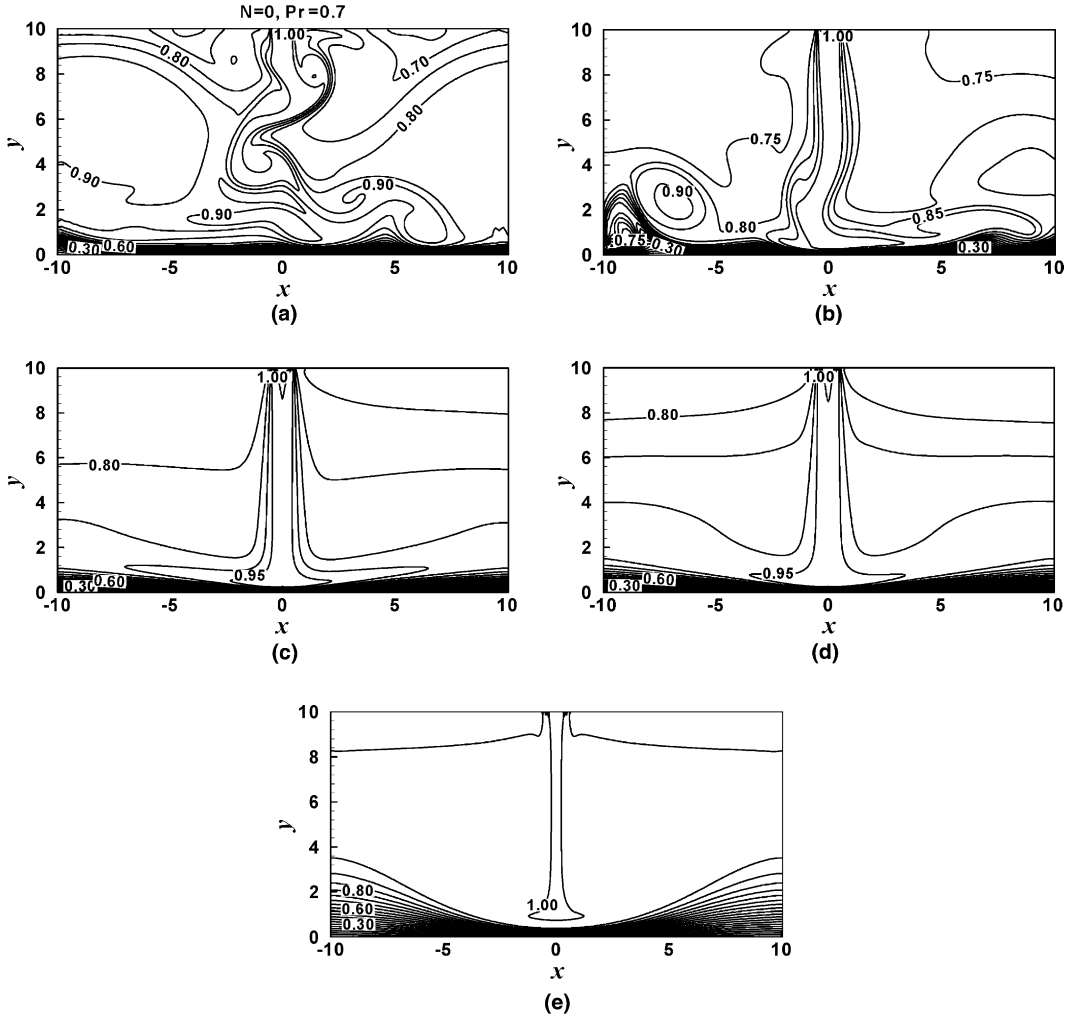

Fig. 8. Instantaneous temperature fields at $Re = 250$, $Pr = 0.7$ and $H/D = 10$ for different N values. (a) $N = 0$, (b) $N = 0.0025$, (c) $N = 0.005$, (d) $N = 0.01$ and (e) $N = 0.03$.

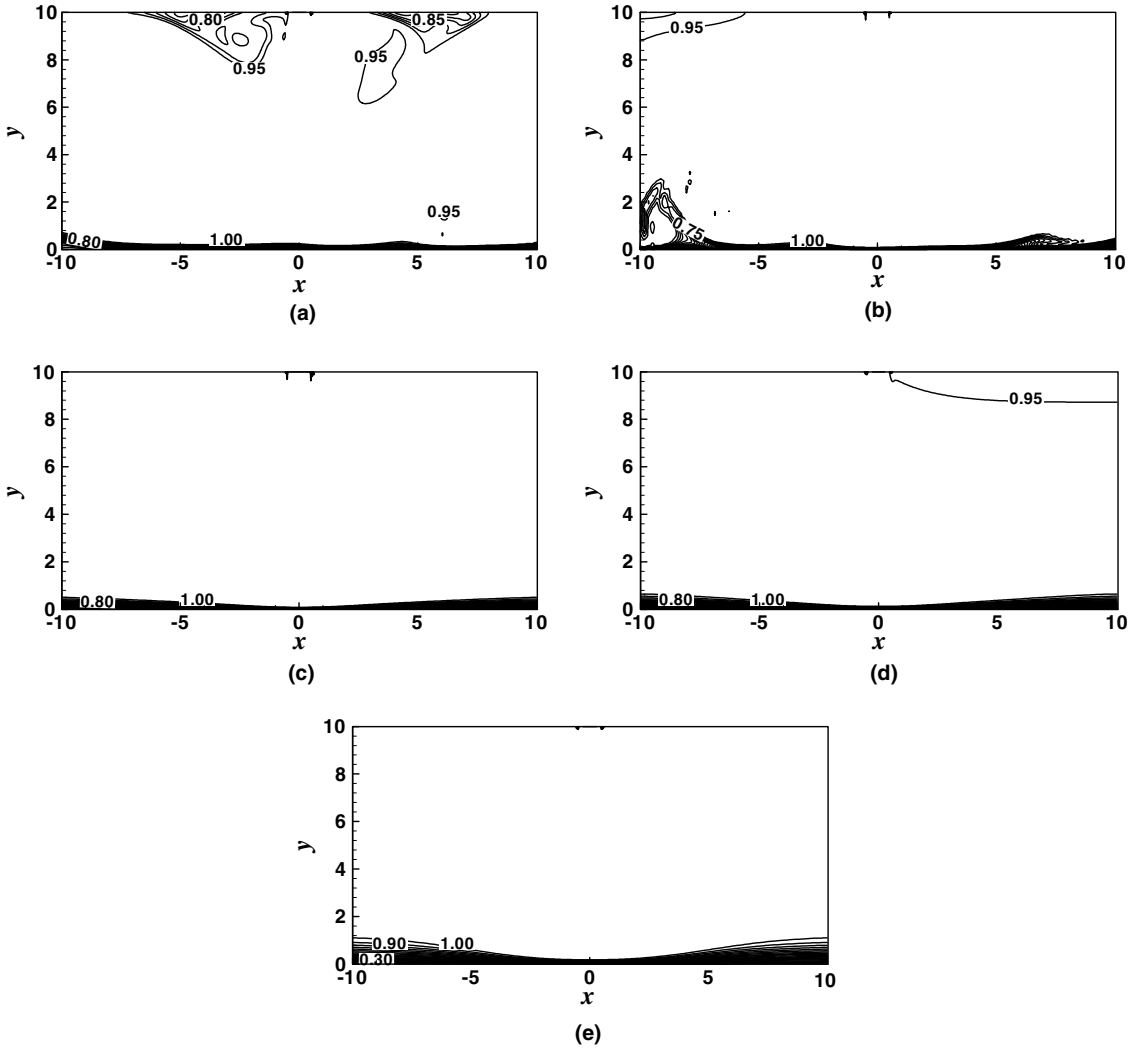

Fig. 9. Instantaneous temperature fields at $Re = 250$, $Pr = 7$ and $H/D = 10$ for different N values. (a) $N = 0$, (b) $N = 0.0025$, (c) $N = 0.005$, (d) $N = 0.01$ and (e) $N = 0.03$.

becomes thinner than those for $Pr = 0.02$. As a result, the thermal gradient and heat transfer rate on the lower wall for $Pr = 0.7$ are larger than those for $Pr = 0.02$. If the Prandtl number increases further to 7 for $N < 0.005$, the thermal boundary layer thickness is much smaller than the hydraulic boundary layer thickness and the temperature fields do not follow the flow fields as shown in Figs. 6 and 9. Thus the value of instantaneous temperature for $N < 0.005$ at $Pr = 7$ is close to 1 in the almost whole region of channel and we can observe the very thin thermal boundary layer close to the lower wall where the temperature changes in the range of 0–1. When $N \geqslant 0.005$, the temperature fields become the steady state with a symmetric pattern with respect to the vertical centerline for different Prandtl numbers of $Pr = 0.02$, 0.7 and 7, because the flow is not time-dependent. If N increases in the range of $N \geqslant 0.005$, the thermal gradient and heat transfer rate on the lower wall decrease because the damping effect of applied magnetic fields increases.

Figs. 10 and 11 show the instantaneous wall pressure coefficient and Nusselt number ($C_{p,\mathrm{stag}}$ and Nu_{stag}) at the stagnation point, respectively, as a function of dimensionless time for different Reynolds numbers at $H/D = 10$ and $Pr = 0.7$ in the absence of applied magnetic fields. When the Reynolds number is 50 and 100, $C_{p,\mathrm{stag}}$ and Nu_{stag} are not time-dependent and have constant values because the fluid flow is steady as above-mentioned. However, if the Reynolds number increases to 175 and 250, $C_{p,\mathrm{stag}}$ and Nu_{stag} change as a function of time because the flow is time-dependent. The amplitude of oscillating $C_{p,\mathrm{stag}}$ and Nu_{stag} at $Re = 250$ is larger

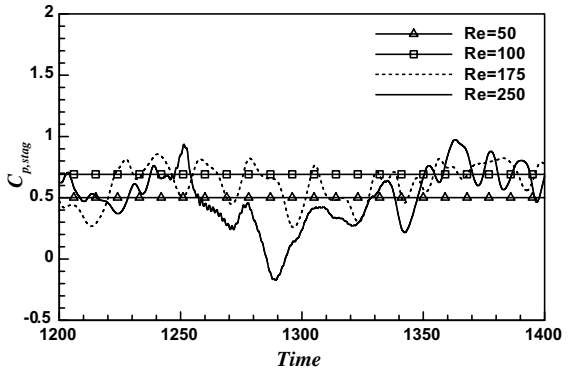

Fig. 10. Instantaneous wall pressure coefficient at the stagnation point ($C_{p,\mathrm{stag}}$) as a function of time for different Reynolds numbers at $H/D = 10$ in the absence of applied magnetic fields.

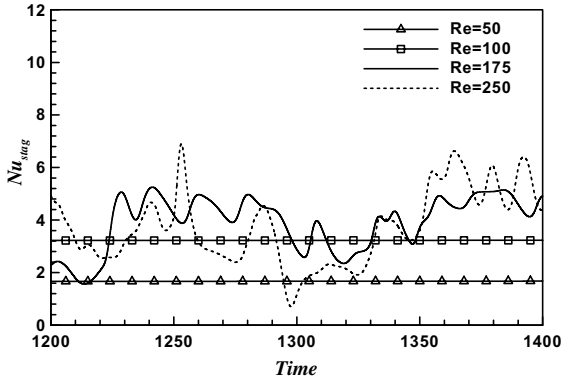

Fig. 11. Instantaneous local Nusselt number at the stagnation point (Nu_{stag}) as a function of time for different Reynolds numbers at $H/D = 10$ and $Pr = 0.7$ in the absence of applied magnetic fields.

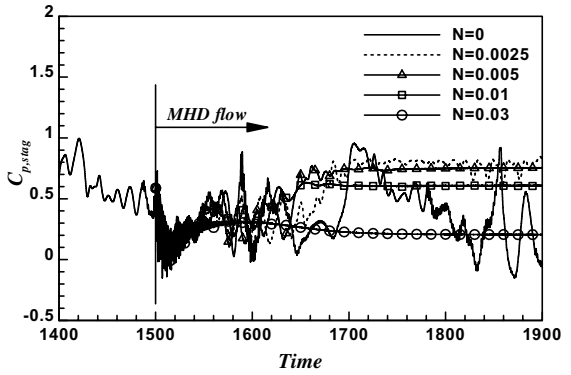

Fig. 12. Instantaneous wall pressure coefficient at the stagnation point ($C_{p,\mathrm{stag}}$) as a function of time for different N values at $H/D = 10$ and $Re = 250$.

than that at $Re = 175$, because the unsteadiness increases with increasing Reynolds number.

Figs. 12 and 13 show the instantaneous wall pressure coefficients and Nusselt number ($C_{p,\mathrm{stag}}$ and Nu_{stag}) for different Prandtl numbers of 0.02, 0.7 and 7 at the stagnation point, respectively, for different values of N as a function of dimensionless time at $H/D = 10$ and $Re = 250$. The time history of $C_{p,\mathrm{stag}}$ and Nu_{stag} during the dimensionless time of $1400 \leqslant t \leqslant 1500$ corresponds

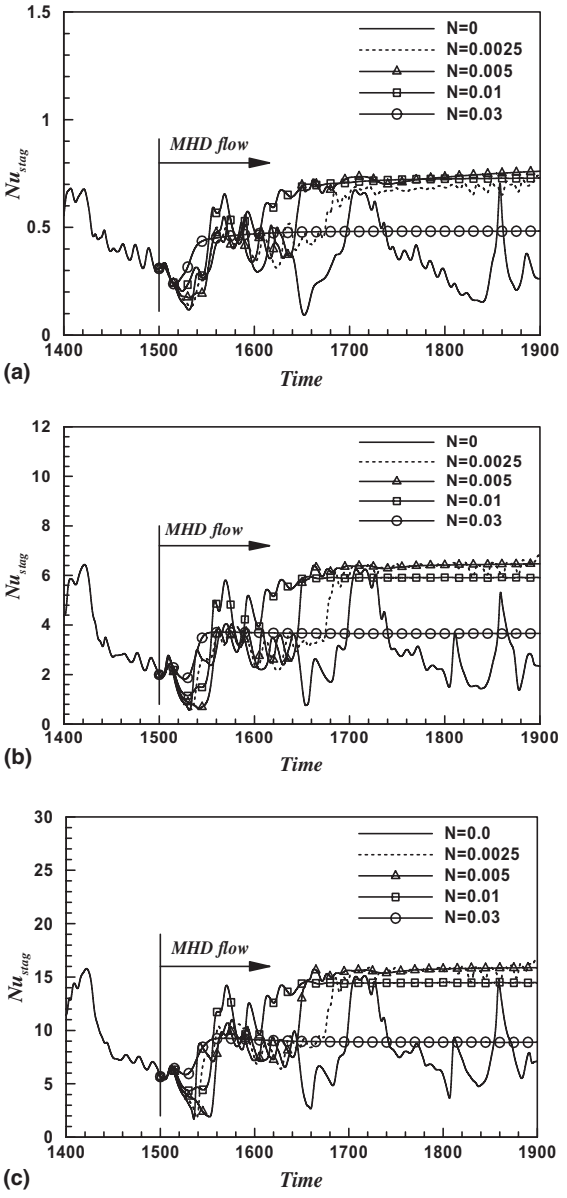

Fig. 13. Instantaneous local Nusselt number at the stagnation point (Nu_{stag}) as a function of time for different N values at $H/D = 10$ and $Re = 250$: (a) $Pr = 0.02$, (b) $Pr = 0.7$ and (c) $Pr = 7$.

to the case without applied magnetic fields ($N = 0$). The flow and temperature fields at $t = 1500$ for the case of $N = 0$ are used as initial conditions to calculate the fluid flow and temperature fields in the presence of applied magnetic fields. The value itself of Nu_{stag} for both cases with and without applied magnetic fields increases with increasing Prandtl number because the thermal boundary layer thickness and thermal gradient on the lower wall increase. However, when the time history of Nu_{stag} changes its shape from the unsteady to the steady pattern as N increases in the presence of magnetic fields, the general trend in the change of Nu_{stag} is generally similar for different Prandtl numbers. If we apply the magnetic field of $N = 0.0025$, the flow is still time-dependent, but the unsteadiness and the oscillating amplitude of $C_{p,\text{stag}}$ and Nu_{stag} decrease very quickly due to the damping effect of applied magnetic fields, compared to the case of $N = 0$ in the absence of applied magnetic field. When the applied magnetic fields increase above $N \geqslant 0.005$, the flow approaches the steady state, and $C_{p,\text{stag}}$ and Nu_{stag} for all three cases of $Pr = 0.02$, 0.7 and 7 reach the constant value.

Figs. 14 and 15 show the time-averaged pressure coefficient and Nusselt number for different Prandtl numbers of 0.02, 0.7 and 7 at the stagnation point ($\overline{C}_{p,\text{stag}}$ and $\overline{Nu}_{\text{stag}}$), respectively, as a function of N at $H/D = 10$ and $Re = 250$. If we increase the strength of applied magnetic field in the unsteady region, the unsteadiness and swinging motion of jet decrease and the jet has more opportunities to impinge on the stagnation point. As a result the values of instantaneous and time-averaged wall pressure coefficients and Nusselt number at the stagnation point increase with increasing N in the presence of relatively weak magnetic fields of $N < 0.005$, and have a maximum value when $N = 0.004$. However, if the flow becomes steady in the presence of relatively strong magnetic field of $N \geqslant 0.005$, the instantaneous and time-averaged wall pressure coefficients and Nusselt number at the stagnation point decrease with increasing N, because the flow cannot reach the stagnation point well and the thickness of thermal boundary layer increases,

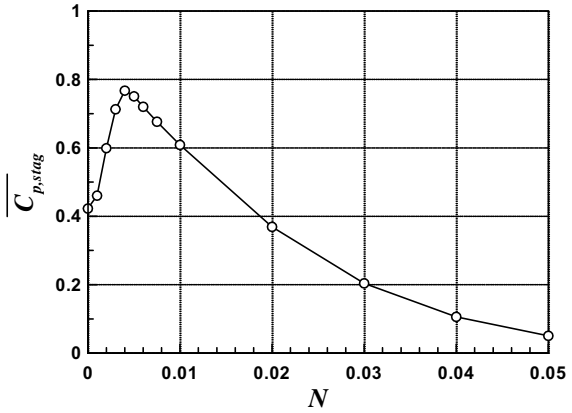

Fig. 14. Time-averaged wall pressure coefficient at the stagnation point ($\overline{C}_{p,\text{stag}}$) as a function of N number at $H/D = 10$ and $Re = 250$.

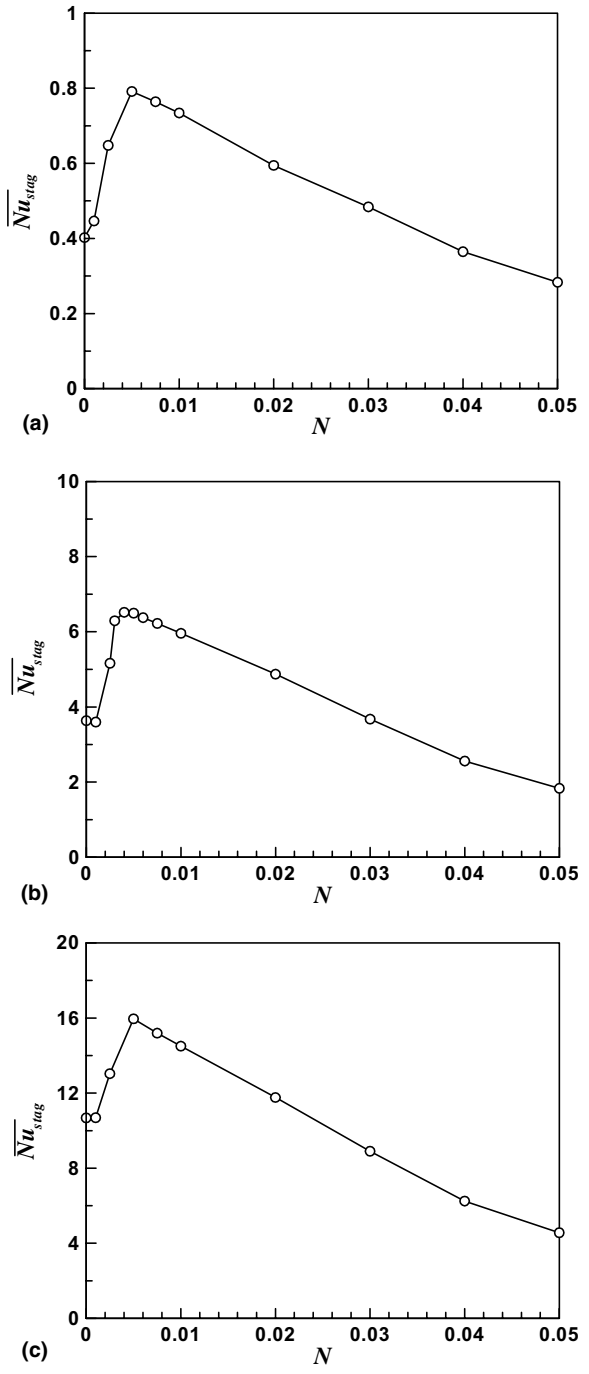

Fig. 15. Time-averaged local Nusselt number at the stagnation point ($\overline{Nu}_{\text{stag}}$) as a function of N number at $H/D = 10$ and $Re = 250$: (a) $Pr = 0.02$, (b) $Pr = 0.7$ and (c) $Pr = 7$.

due to increasing damping effect of magnetic field in the presence of strong magnetic fields. Similar to Nu_{stag}, the absolute magnitude of $\overline{Nu}_{stag}$ depends on the Prandtl number and increases with increasing Prandtl number due to increasing thermal boundary layer thickness.

5. Conclusions

The present study numerically investigates the characteristics of two-dimensional fluid flow and heat transfer in the confined impinging jet in the presence of magnetic fields. Numerical simulations to calculate the flow and thermal fields in the confined jet are carried out for different Reynolds and Prandtl numbers in the presence of applied magnetic fields. The results with the applied magnetic fields are compared with those without magnetic fields in order to investigate the effects of applied magnetic fields on the fluid flow and heat transfer characteristics in the confined jet.

When the uniform magnetic fields normal to the channel are applied to the jet flow, the Lorentz force acting on the flow damps the flow oscillation caused by the vortex shedding. As a result, the jet flow oscillation in the channel is first weakened, eventually resulting in a steady and symmetric flow. There exists the critical Stuart number, which makes the time-dependent fluid flow and temperature fields steady, depending on the Reynolds number.

As the Stuart number increases in the range of $N < 0.005$ when $H/D = 10$ and $Re = 250$, the flow and temperature fields are time-dependent, the unsteadiness and swinging motion of jet decrease and the jet has more opportunities to impinge on the stagnation point. As a result the values of instantaneous and time-averaged wall pressure coefficients and Nusselt number at the stagnation point increase with increasing N in the range of $N < 0.005$.

As the Stuart number increases further in the range of $N \geqslant 0.005$ when $H/D = 10$ and $Re = 250$, the flow and temperature fields become a steady state. The damping effect of applied magnetic field on the confined jet flow increases with increasing Stuart number in the steady region, making the strength of jet impinging on the lower wall weaker. As a result, the instantaneous and time-averaged wall pressure coefficients and Nusselt number at the stagnation point decrease with increasing Stuart number in the unsteady region.

Acknowledgement

Prof. Yoon thanks for the financial support by Advanced Ship Engineering Research Center (ASERC) of Pusan National University through Korea Science and Engineering Foundation.

References

[1] E.M. Sparrow, T.C. Wong, Impingement transfer coefficients due to initially laminar slot jets, Int. J. Heat Mass Transfer 18 (1975) 597–605.
[2] M. Bouainnouche, N. Bourabaa, B. Desmet, Numerical Study of the wall shear stress produced by the impingement of a plane turbulent jet on a plate, Int. J. Numer. Method Heat Fluid Flow 7 (8) (1997) 548–564.
[3] M. Chen, R. Chalupa, A.C. West, V. Modi, High Schmidt mass transfer in a laminar impinging slot jet flow, Int. J. Heat Mass Transfer 43 (2000) 3907–3915.
[4] A.H. Beitelmal, M.A. Saad, C.D. Patel, The effect of inclination on the heat transfer between a flat surface and an impinging two-dimensional air jet, Int. J. Heat Fluid Flow 21 (2000) 156–163.
[5] D.J. Phares, G.T. Smedley, R.C. Flagan, The wall shear stress produced by the normal impingement of a jet on a flat surface, J. Fluid Mech. 418 (2000) 351–375.
[6] H. Chattopadhyay, S.K. Saha, Numerical investigation of heat transfer over a moving surface due to impinging knife-jets, Numer. Heat Transfer, Part A 39 (2001) 531–549.
[7] S.D. Hwang, C.H. Lee, H.H. Cho, Heat transfer and flow structure in axisymmetric impinging jet controlled by vortex paring, Int. J. Heat Fluid Flow 22 (2001) 293–300.
[8] Y. Choo, B. Kang, The velocity distribution of the liquid sheet formed by two low-speed impinging jets, Phys. Fluids 14 (2) (2002) 622–627.
[9] L.B.Y. Aldabbagh, I. Sezai, Numerical simulation of three-dimensional laminar multiple impinging square jets, Int. J. Heat Fluid Flow 23 (2002) 509–518.
[10] V.C. Chiriac, A. Ortega, A numerical study of the unsteady flow and heat transfer in a transitional confined slot jet impinging on an isothermal surface, Int. J. Heat Mass Transfer 45 (2002) 1237–1248.
[11] Y.M. Chung, K.H. Luo, N.D. Sandham, Numerical study of momentum and heat transfer in unsteady impinging jets, Int. J. Heat Fluid Flow 23 (2002) 592–600.
[12] F. Beaubert, S. Viazzo, Large eddy simulation of plane turbulent impinging jets at moderate Reynolds numbers, Int. J. Heat Fluid Flow 24 (2003) 512–519.
[13] H. Chattopadhyay, S.K. Saha, Turbulent flow and heat transfer from a slot jet impinging on a moving plate, Int. J. Heat Fluid Flow 24 (2003) 685–697.
[14] M.Y. Ha, H.G. Lee, S.H. Seong, Numerical simulation of three-dimensional flow, heat transfer, and solidification of steel in continuous casting mold with electromagnetic brake, J. Mater. Process. Technol. 133 (2003) 322–339.
[15] B. Mück, C. Günther, U. Müller, L. Bühler, Three-dimensional MHD flows in rectangular ducts with internal obstacles, J. Fluid Mech. 418 (2000) 265–295.
[16] H.S. Yoon, H.H. Chun, M.Y. Ha, H.G. Lee, A numerical study on the fluid flow and heat transfer around a circular cylinder in an aligned magnetic fields, Int. J. Heat Mass Transfer 47 (2004) 4075–4087.
[17] J. Kim, P. Moin, Application of a fractional-step method to incompressible Navier–Stokes equations, J. Comp. Phys. 59 (1985) 308–323.
[18] P.S. Pacheco, Parallel Programming with MPI, Morgan kaufmann Publishers Inc., 1997.